Additional illustrations of NL-SAR method for resolution-preserving (Pol)(In)SAR denoising

Charles-Alban Deledalle, Loïc Denis, Florence Tupin, Andreas Reigber, Marc Jäger

Additional illustrations of NL-SAR method for resolution-preserving (Pol)(In)SAR denoising

Charles-Alban Deledalle, Loïc Denis, Florence Tupin, Andreas Reigber, and Marc Jäger

— About this document —

This document provides additional information and results of the method NL-SAR described in our paper: "NL-SAR: a unified Non-Local framework for resolution-preserving (Pol)(In)SAR denoising" submitted to *IEEE Trans. on Geoscience and Remote Sensing* [Deledalle et al., 2013]. NL-SAR is a fully automatic method for speckle reduction that handles amplitude, polarimetric and/or interferometric SAR data. It can process single look and multi-look images. The source code of the method is freely available at:
http://www.math.u-bordeaux1.fr/~cdeledal/nlsar.php.

— Structure of the document —

The first part of the document provides some justifications for the design choices done in NL-SAR. The second part gives numerous results of NL-SAR on both simulated and real SAR images.

C. Deledalle is with IMB, CNRS-Université Bordeaux 1, Talence, France, e-mail: charles-alban.deledalle@math.u-bordeaux1.fr
L. Denis is with the Laboratoire Hubert Curien, UMR 5516 CNRS, Université de Saint-Etienne and Telecom Saint-Etienne; Saint-Etienne, France e-mail: loic.denis@uni-st-etienne.fr.
F. Tupin is with Institut Mines-Telecom, Telecom ParisTech, CNRS LTCI, Paris, France, e-mail: florence.tupin@telecom-paristech.fr.
A. Reigber and M. Jäger are with the Microwaves and Radar Institute, German Aerospace Center (DLR), Wessling D-82234, Germany, e-mail: {andreas.reigber,marc.jaeger}@dlr.de.

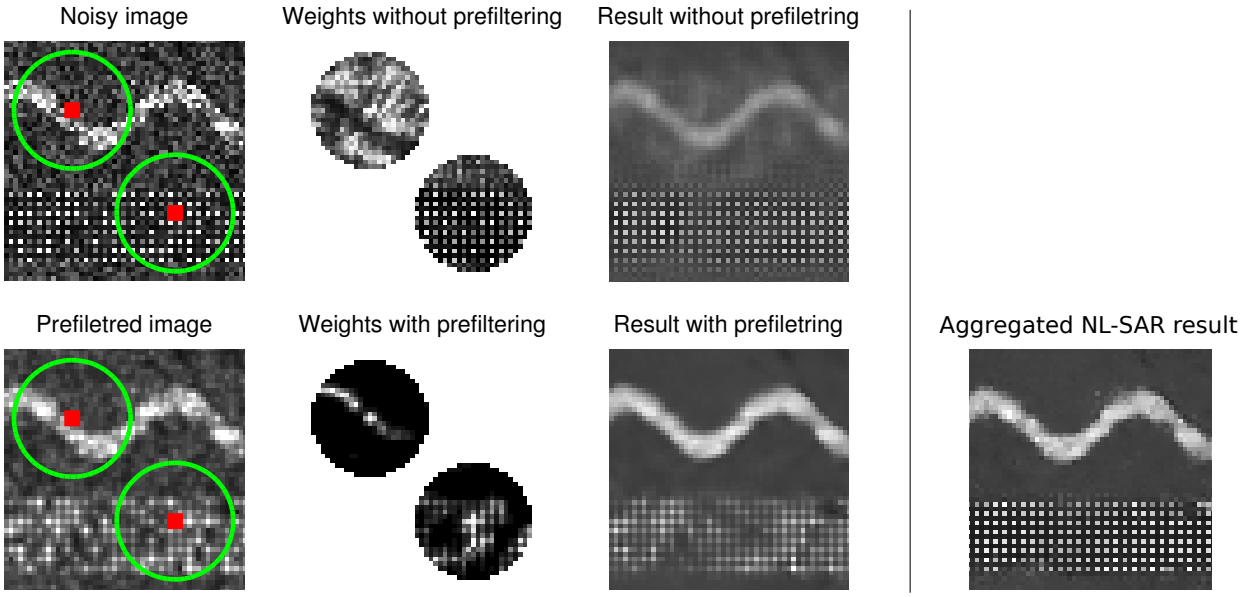

Fig. 1. (left) Top: non local means result by comparing 7×7 patches extracted from the noisy image. Bottom: Same except patches are extracted in a prefiltered image. Two pixels of interest (in red) are focused and their associated weights in the circle searching window (in green) are displayed. (right) NL-SAR result that is an aggregation of several non local means results obtained for different prefiltering strengths, patch sizes and search window sizes.

1. Justification of some design choices

This document cannot substitute for the full description of NL-SAR method given in the paper "NL-SAR: a unified Non-Local framework for resolution-preserving (Pol)(In)SAR denoising". We only recall here the general scheme of the method before illustrating some of the steps:

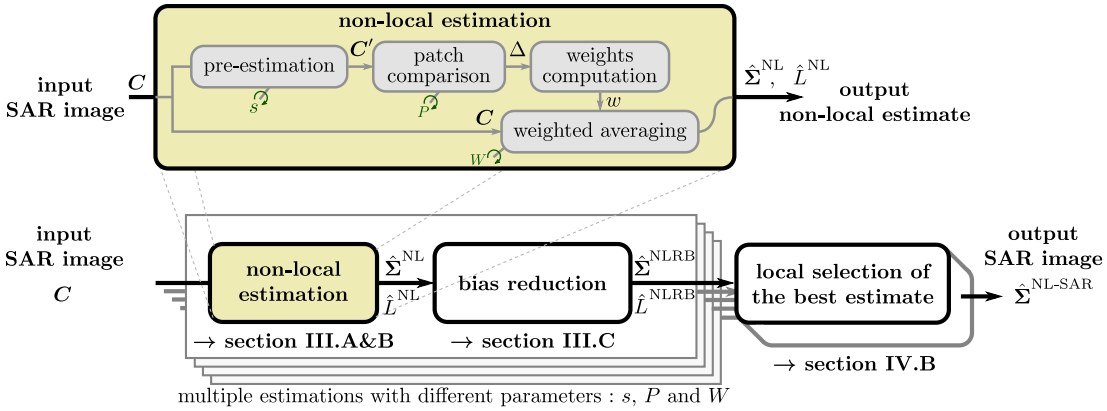

1.1. Pre-estimation

Pre-filtering[1] can help to better discriminate between similar and dissimilar patches. However, since it introduces some blurring, it is not beneficial to high frequency structures/point-like objects. A rather coarse pre-filtering method can be used in NL-SAR because the final result of the method is obtained after local selection of the best amount of smoothing. Figure 1 illustrates that the local selection step successfully chooses the results obtained with weights computed on the pre-filtered image in regions where it improves the discrimination, and relies on the results without pre-filtering in other regions. Note that pre-filtering impacts only the computation of weights and that the weighted combination is performed on the original data.

[1]in NL-SAR, pre-filtering is just a simple convolution with a truncated Gaussian kernel

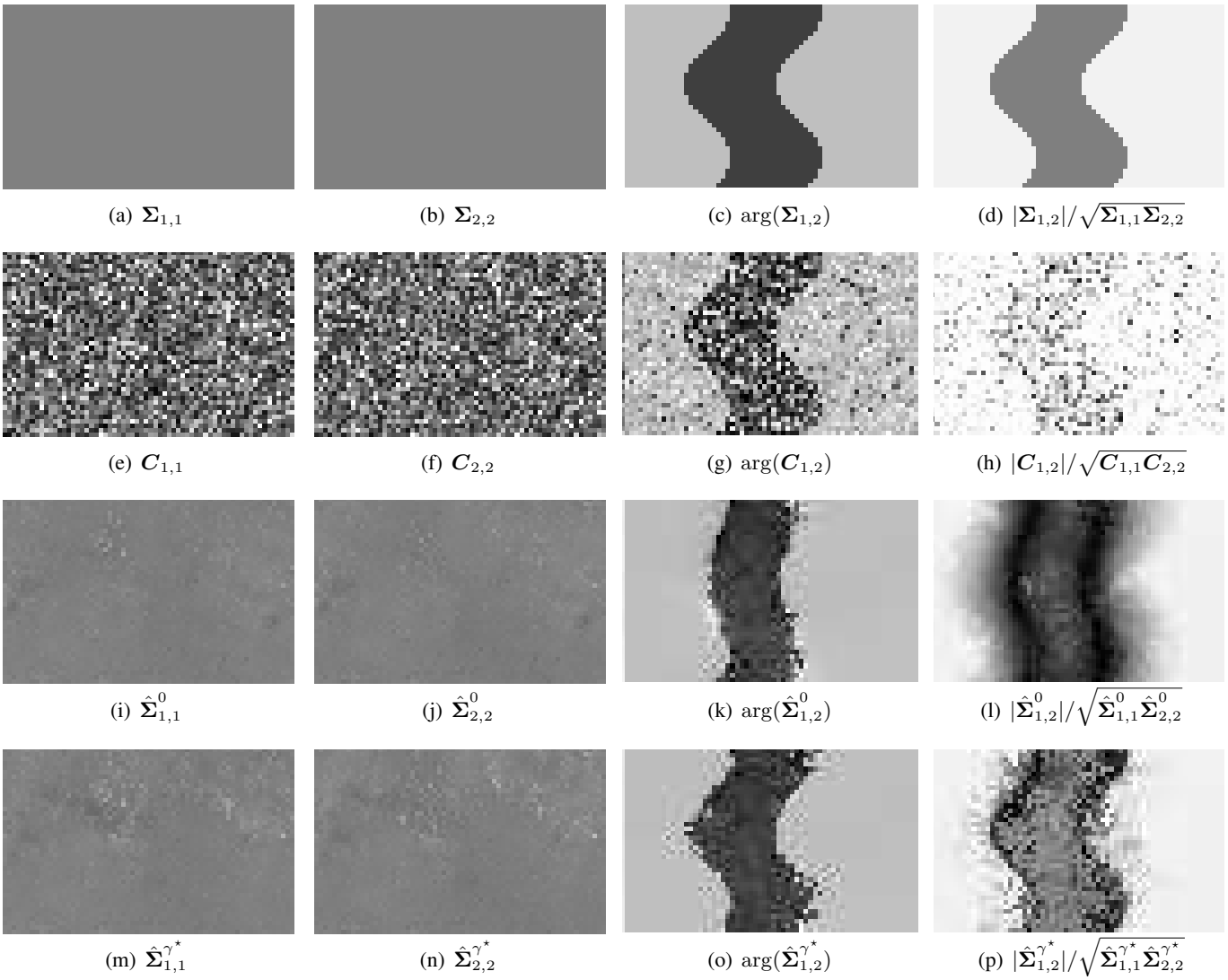

(a) $\mathbf{\Sigma}_{1,1}$ (b) $\mathbf{\Sigma}_{2,2}$ (c) $\arg(\mathbf{\Sigma}_{1,2})$ (d) $|\mathbf{\Sigma}_{1,2}|/\sqrt{\mathbf{\Sigma}_{1,1}\mathbf{\Sigma}_{2,2}}$

(e) $\boldsymbol{C}_{1,1}$ (f) $\boldsymbol{C}_{2,2}$ (g) $\arg(\boldsymbol{C}_{1,2})$ (h) $|\boldsymbol{C}_{1,2}|/\sqrt{\boldsymbol{C}_{1,1}\boldsymbol{C}_{2,2}}$

(i) $\hat{\mathbf{\Sigma}}^0_{1,1}$ (j) $\hat{\mathbf{\Sigma}}^0_{2,2}$ (k) $\arg(\hat{\mathbf{\Sigma}}^0_{1,2})$ (l) $|\hat{\mathbf{\Sigma}}^0_{1,2}|/\sqrt{\hat{\mathbf{\Sigma}}^0_{1,1}\hat{\mathbf{\Sigma}}^0_{2,2}}$

(m) $\hat{\mathbf{\Sigma}}^{\gamma^\star}_{1,1}$ (n) $\hat{\mathbf{\Sigma}}^{\gamma^\star}_{2,2}$ (o) $\arg(\hat{\mathbf{\Sigma}}^{\gamma^\star}_{1,2})$ (p) $|\hat{\mathbf{\Sigma}}^{\gamma^\star}_{1,2}|/\sqrt{\hat{\mathbf{\Sigma}}^{\gamma^\star}_{1,1}\hat{\mathbf{\Sigma}}^{\gamma^\star}_{2,2}}$

Fig. 2. Results on a simulated image with 2×2 covariance matrices in 1 look (case where $L < D$). From top to bottom: underlying information, noisy version, restoration with $\gamma = 0$, restoration with the proposed $\gamma^\star = (L/D)^{1/3} \approx 0.8$.

1.2. Patch comparison

Estimation of the similarity between two empirical covariance matrices $\boldsymbol{C}_1$ and $\boldsymbol{C}_2$ is difficult when the matrix dimension D is larger than the number of looks L. Matrices $\boldsymbol{C}_1$ and $\boldsymbol{C}_2$ are then singular and their probability density function is no more given by Wishart distribution.

The similarity criterion given by the generalized likelihood ratio under Wishart likelihood is defined as a ratio of determinants:

$$\mathcal{L}_G(\boldsymbol{C}'_1, \boldsymbol{C}'_1) = \frac{|\boldsymbol{C}'_1|^{L'} \cdot |\boldsymbol{C}'_2|^{L'}}{|\frac{1}{2}(\boldsymbol{C}'_1 + \boldsymbol{C}'_2)|^{2L'}} \ . \tag{1}$$

This criterion must be adapted in the case of $D > L$. A satisfying similarity criterion should be sensitive to changes in intensities, interferometric phase or polarimetric properties.

We illustrate in the case of interferometry (i.e., $D = 2$) that the criterion we use in NL-SAR is better behaved than some alternate solutions, namely the computation of the determinants in equation (1) using only the largest eigenvalue, or skipping null eigenvalues.

The empirical covariance matrix estimated from a pair of single look complex images is given by:

$$\hat{\Sigma}_p = C_p = \begin{pmatrix} I_p & \sqrt{I_p I'_p} e^{j\phi_p} \\ \sqrt{I_p I'_p} e^{-j\phi_p} & I'_p \end{pmatrix} \tag{2}$$

where the two complex values at pixel p are $\sqrt{I_p}e^{j(\psi_p+\phi_p)}$ and $\sqrt{I'_p}e^{j\psi_p}$. The first eigenvalue of this rank-one covariance matrix is:

$$\lambda_{p1} = I_p + I'_p\,. \tag{3}$$

The empirical covariance matrix estimated from the two locations 1 and 2 is:

$$\hat{\Sigma}_{12} = \frac{1}{2}(C_1 + C_2) = \frac{1}{2}\begin{pmatrix} I_1 + I_2 & \sqrt{I_1 I'_1}e^{j\phi_1} + \sqrt{I_2 I'_2}e^{j\phi_2} \\ \sqrt{I_1 I'_1}e^{-j\phi_1} + \sqrt{I_2 I'_2}e^{-j\phi_2} & I'_1 + I'_2 \end{pmatrix} \tag{4}$$

whose eigenvalues are roots of $\lambda^2 - \mathrm{Tr}(\hat{\Sigma}_{12})\lambda + |\hat{\Sigma}_{12}|$, hence, its 1st eigenvalue is

$$(\lambda_{12})_1 = \frac{\mathrm{Tr}(\hat{\Sigma}_{12}) + \sqrt{\mathrm{Tr}(\hat{\Sigma}_{12})^2 - 4|\hat{\Sigma}_{12}|}}{2}. \tag{5}$$

If only the largest eigenvalue is used in place of the determinants in equation (1), the similarity criterion writes:

$$c(\boldsymbol{C}_1, \boldsymbol{C}_2) = \frac{(\lambda_1)_1^2 (\lambda_2)_1^2}{|(\lambda_{12})_1|^2}\,. \tag{6}$$

Since the determinant $|\hat{\Sigma}_{12}|$ can be expanded as

$$|\hat{\Sigma}_{12}| = \frac{I_1 I'_2 + I_2 I'_1 - 2\sqrt{I_1 I'_1 I_2 I'_2}\cos(\phi_1 - \phi_2)}{4}\,, \tag{7}$$

for given values of I_1, I'_1, I_2 and I'_2, the determinant decreases when ϕ_1 and ϕ_2 become closer. Hence, the similarity criterion (6) mistakenly indicates that covariance matrices at locations 1 and 2 are more dissimilar when the interferometric phases ϕ_1 and ϕ_2 are actually getting closer.

The following alternative similarity criterion suffers from insensibility to some intensity changes:

$$c(\boldsymbol{C}_1, \boldsymbol{C}_2) = \frac{(\lambda_1)_1^2 (\lambda_2)_1^2}{|\hat{\Sigma}_{12}|^2} = \frac{16(I_1 + I'_1)^2 (I_2 + I'_2)^2}{(I_1 I'_2 + I_2 I'_1 - 2\sqrt{I_1 I'_1 I_2 I'_2}\cos(\phi_1 - \phi_2))^2}\,. \tag{8}$$

Indeed, for all $\alpha > 0$,

$$c(\boldsymbol{C}_1, \boldsymbol{C}_2) = c(\boldsymbol{C}_1, \alpha\boldsymbol{C}_2)\,. \tag{9}$$

The similarity criterion used in NL-SAR behaves in a more favorable way. Indeed, by weighting off-diagonal terms of the covariance matrices by γ, the similarity criterion becomes:

$$\mathcal{L}_G(\boldsymbol{C}_1, \boldsymbol{C}_2) \propto \frac{|\hat{\boldsymbol{C}}'_1||\hat{\boldsymbol{C}}'_2|}{|\hat{\boldsymbol{C}}'_1 + \hat{\boldsymbol{C}}'_2|^2} = \frac{(I_1 I'_1 I_2 I'_2)(1-\gamma^2)}{(I_1 I'_2 + I_2 I'_1 + (1-\gamma^2)(I_1 I'_1 + I_2 I'_2) - 2\gamma^2\sqrt{I_1 I'_1 I_2 I'_2}\cos(\phi_1 - \phi_2))^2} \tag{10}$$

Note that when $\gamma \to 1$, we have, for any $\alpha > 0$:

$$\frac{\mathcal{L}_G(\boldsymbol{C}_1, \boldsymbol{C}_2)}{1-\gamma^2} \to \frac{\mathcal{L}_G(\boldsymbol{C}_1, \alpha\boldsymbol{C}_2)}{1-\gamma^2} \tag{11}$$

meaning that we are no more discriminant in intensities. When $\gamma \to 0$, we are obviously no more discriminant in phase. For $0 < \gamma < 1$, we have

$$-\log \mathcal{L}_G(\boldsymbol{C}_1, \boldsymbol{C}_2) \propto \log\left(\frac{I_1 I'_2 + I_2 I'_1 + (1-\gamma^2)(I_1 I'_1 + I_2 I'_2) - 2\gamma^2\sqrt{I_1 I'_1 I_2 I'_2}\cos(\phi_1 - \phi_2)}{\sqrt{I_1 I'_1 I_2 I'_2}}\right) \tag{12}$$

$$\propto \log\left(\underbrace{\left(\sqrt{\frac{I_1}{I_2}} + \sqrt{\frac{I_2}{I_1}}\right)\left(\sqrt{\frac{I'_1}{I'_2}} + \sqrt{\frac{I'_2}{I'_1}}\right)}_{\text{intensity dissimilarity}} - \gamma^2 \underbrace{\left(\sqrt{\frac{I_1 I'_1}{I_2 I'_2}} + \sqrt{\frac{I_2 I'_2}{I_1 I'_1}}\right)}_{\text{correction}} + 2\gamma^2 \underbrace{(-\cos(\phi_1 - \phi_2))}_{\text{phase dissimilarity}}\right) \tag{13}$$

The first term decreases when intensities I_1 and I'_1 gets closer to I_2 and I'_2 respectively. The second term seems to compensate for inter-channel correlations. The last term decreases when phases ϕ_1 and ϕ_2 get closer. This criterion clearly measures both the dissimilarity in intensity and in interferometric phase. Figure 2 illustrates that the criterion used in NL-SAR can discriminate changes in interferometric phase even if no change occur in amplitude compared to an intensity-only criterion.

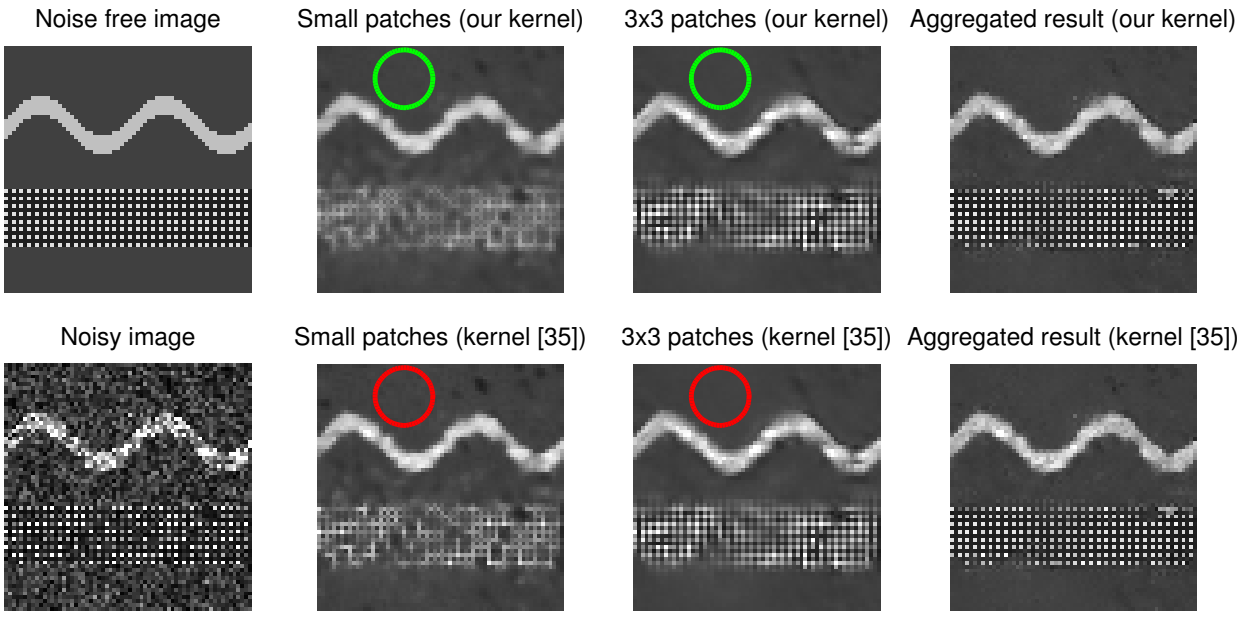

Fig. 3. Comparisons between kernels that adapt to the distribution of the criterion versus kernel based on moments of the criterion only (similar to the one of [Kervrann and Boulanger, 2008], refereed in the figure to as [35]). Green circles illustrates that the first kernels ensure a same level of noise reduction in homogeneous regions, while red kernels illustrates that the second kernel does not.

1.3. Weights computation

Fig. 3 gives an illustration that kernels adapted to the distribution can preserve a same level of noise reduction in homogeneous areas compared to other kernels. The smoothness level in the aggregated result is then controlled.

We can observe that the resulting aggregated results are however not that much different. The most significant advantage of our kernel is that no manual tuning is required. In comparison, the kernel of [Kervrann and Boulanger, 2008] is parametrized and this parameter (namely the α quantile) has been set by hand to 0.99 but should/could be tuned differently for other levels of noise or to favor specific patch sizes.

1.4. Unbiasedness of WMLE with GLR based weights

Adaptive selection of pixel values can lead to selection bias as observed for some speckle reduction methods [Lee, 1983], [Vasile et al., 2006] and studied in [Lee et al., 2009]. Due to speckle noise, intensities follow a heavy-tailed distribution and selecting pixels with similar intensities discards large values which biases the subsequent maximum likelihood estimation. This bias depends strongly on how the similarity criterion is defined. We remark that GLR does not induce bias. The explanations is detailed below.

Given i.i.d. observations $I' = Rs$ where R is the underlying reflectivity and s is a random variable modeling speckle with a Gamma distribution, [Lee et al., 2009] explain that an unbiased estimate of R can be obtained by averaging observations I' that fall in an interval $[\epsilon, \epsilon']$ such that:

$$\mathbb{E}[\hat{R}] = \frac{\displaystyle\int_{\epsilon}^{\epsilon'} I' p(I'|R)\, \mathrm{d}I'}{\displaystyle\int_{\epsilon}^{\epsilon'} p(I'|R)\, \mathrm{d}I'} = R\,. \tag{14}$$

In [Lee et al., 2009], it is shown that it is not possible to solve Eq. (14) directly, i.e., to get a closed-form expression for ϵ and ϵ'. A numerical search technique is then used with an iterative algorithm to estimate ϵ and ϵ'.

In this scenario, ϵ and ϵ' are deterministic values, functions of the unknown value R of the pixel of interest, which in [Lee et al., 2009] is replaced by the estimate obtained thanks to a 3×3 boxcar filter. However, we remark that in their original forms, the sigma, bilateral or NLmeans filters compare noisy values I and I' directly instead of a noisy value I' against a pre-estimation of R. We then should consider to select pixel candidates with values I' lying in a non-deterministic selection range of the form $[\epsilon(I), \epsilon'(I)]$ depending of the observed intensity I of the

TABLE I
PSNR / SSIM

Method	L = 1	L = 2	L = 4	L = 16	L = 1	L = 2	L = 4	L = 16
	House				Mandrill			
Noisy	-3.54 / 0.098	-0.78 / 0.157	2.13 / 0.229	8.13 / 0.437	-3.72 / 0.422	-0.93 / 0.552	1.99 / 0.675	7.94 / 0.862
Pretest	9.02 / 0.613	11.50 / 0.724	13.86 / 0.793	17.62 / 0.858	4.89 / 0.514	6.03 / 0.629	7.11 / 0.748	10.47 / 0.900
PPB	10.30 / 0.647	12.78 / 0.727	14.47 / 0.782	17.34 / 0.853	4.99 / 0.500	6.11 / 0.623	7.61 / 0.754	10.40 / 0.900
NL-SAR	11.05 / 0.690	12.77 / 0.749	14.70 / 0.799	18.24 / 0.862	5.45 / 0.594	6.57 / 0.692	7.97 / 0.778	11.83 / 0.913
SARBM3D	**12.29 / 0.746**	**14.42 / 0.794**	**16.09 / 0.828**	**19.37 / 0.883**	**6.06 / 0.649**	**7.33 / 0.749**	**8.83 / 0.832**	**12.09 / 0.929**
	Mire				Mosaic			
Noisy	0.37 / 0.536	3.17 / 0.646	6.05 / 0.745	12.04 / 0.899	-1.56 / 0.240	1.25 / 0.322	4.11 / 0.412	10.10 / 0.604
Pretest	9.07 / 0.928	12.23 / 0.974	14.64 / 0.988	19.59 / 0.996	6.61 / 0.605	7.92 / 0.711	9.62 / 0.810	13.16 / 0.925
PPB	10.56 / 0.953	12.45 / 0.973	14.40 / 0.984	18.81 / 0.994	7.03 / 0.614	8.40 / 0.697	9.99 / 0.785	12.73 / 0.898
NL-SAR	11.25 / 0.957	15.39 / 0.984	**19.87 / 0.994**	**25.77 / 0.999**	8.53 / 0.691	9.88 / 0.769	11.67 / 0.846	**15.82 / 0.947**
SARBM3D	**12.98 / 0.969**	**15.79 / 0.986**	18.14 / 0.992	22.61 / 0.998	**8.80 / 0.720**	**10.06 / 0.791**	**11.75 / 0.863**	15.26 / 0.946

pixel of interest such that

$$\mathbb{E}[\hat{R}] = \frac{\displaystyle\int_{\mathbb{R}^+} \left(\int_{\epsilon(I)}^{\epsilon'(I)} I' p(I'|R) \, \mathrm{d}I' \right) \, p(I|R) \, \mathrm{d}I}{\displaystyle\int_{\mathbb{R}^+} \left(\int_{\epsilon(I)}^{\epsilon'(I)} p(I'|R) \, \mathrm{d}I' \right) \, p(I|R) \, \mathrm{d}I} = R \, . \tag{15}$$

The choice $\epsilon(I) = I/\zeta$ and $\epsilon'(I) = I\zeta$ for some $\zeta > 1$ fulfills the unbiasedness condition defined by Eq. (15), i.e., provides a selection rule leading to an unbiased estimate of R (irrespectively of the number of looks that parametrized the gamma distribution). Of course this result still holds when considering a soft selection (*i.e.*, with weights), since one can expressed the result of soft-selection based estimation as an (infinite) convex combination of (unbiased) hard-selection based estimates obtained for each level set of the kernel function, thus leading to an unbiased estimate. Hence, any similarity criterion δ that verifies

$$\forall \gamma > 0, \quad \exists \zeta > 0 \quad \text{such that} \quad \{I' | \delta(I, I') \leq \gamma\} = [I/\zeta, I\zeta]$$

provides a selection rule leading to an unbiased estimation. This is in particular the case of $\mathcal{L}_G$. Note that this result can be extended to selection based on patch comparison, under an independence assumption of patch values: $\Delta(x, x') = \sum_\tau - \log \mathcal{L}_G[I(x+\tau), I(x'+\tau)] = - \log \mathcal{L}_G[I(x), I(x')] + C$ where C is independent of $I(x)$ and $I(x')$.

2. Additional results

2.1. Amplitude images

We give some additional illustrations of how NL-SAR compares to state-of-the-art speckle reduction methods when applied to amplitude images.

a) Qualitative and quantitative performance on some reference images:

Figure 4 and 5 compare the results of NL-SAR with iterative PPB [Deledalle et al., 2009] and SAR-BM3D [Parrilli et al., 2012] in the case of low signal-to-noise ratio (single look images, figure 4) and good signal-to-noise ratio (16 looks images, figure 5). The performance of each method is compared in terms of PSNR and SSIM in table I. These images can help identify what kind of artifact is introduced by each method.

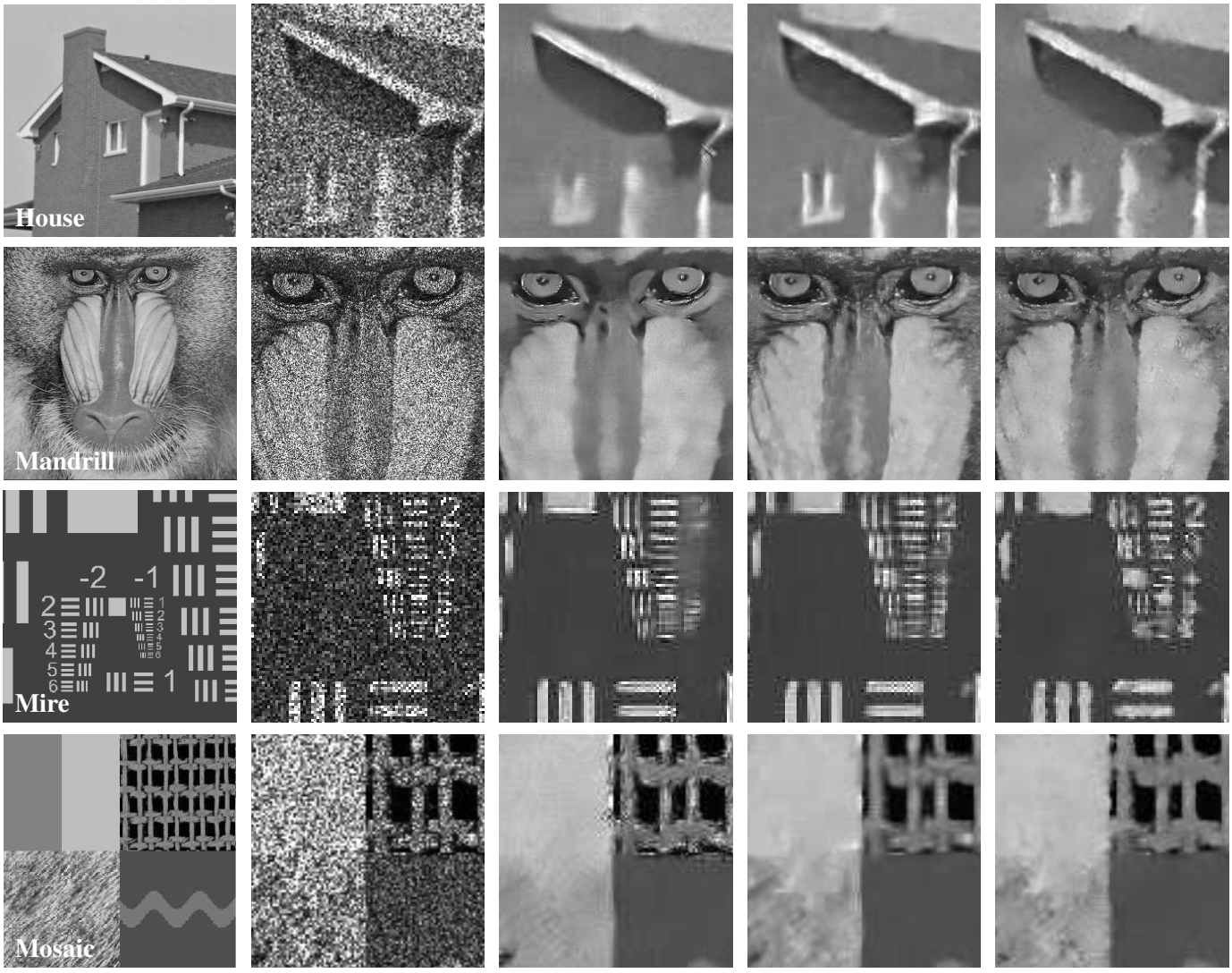

(a) True image (b) Noisy image (c) It. PPB filter (d) SAR-BM3D (e) NL-SAR

Fig. 4. Illustration on denoising scalar (intensity) simulated images. (a) True image. (b) Noisy image (L=1). (c) It. PPB filter. (d) SAR-BM3D. (e) Our result.

b) Results obtained with the benchmark methodology of [Di Martino et al., 2013]:

Figure 6 and table II give the result of NL-SAR on the 5 test cases proposed in [Di Martino et al., 2013] to evaluate the performance of speckle reduction methods. We invite the interested reader to refer to [Di Martino et al., 2013] for a detailed description of each criterion. Even though NL-SAR does not perform best on this benchmark, it is in a par with other state-of-the-art methods (namely PPB and SARBM3D), often belonging in the top two ranked methods.

c) Results on satellite SAR image:

In figure 7, NL-SAR and IDAN [Vasile et al., 2006] are applied to a ERS-1 SAR image to compare their performance for speckle reduction. In figure 8, NL-SAR and IDAN [Vasile et al., 2006] are applied to a TerraSAR-X image to compare their performance for speckle reduction.

2.2. InSAR images

Figures 9 and 10 compare IDAN [Vasile et al., 2006] and NL-SAR on aerial interferometric SAR images. Figures 11 and 12 give results obtained with IDAN, refined Lee [Lee et al., 2003] and NL-SAR on satellite interferometric SAR images

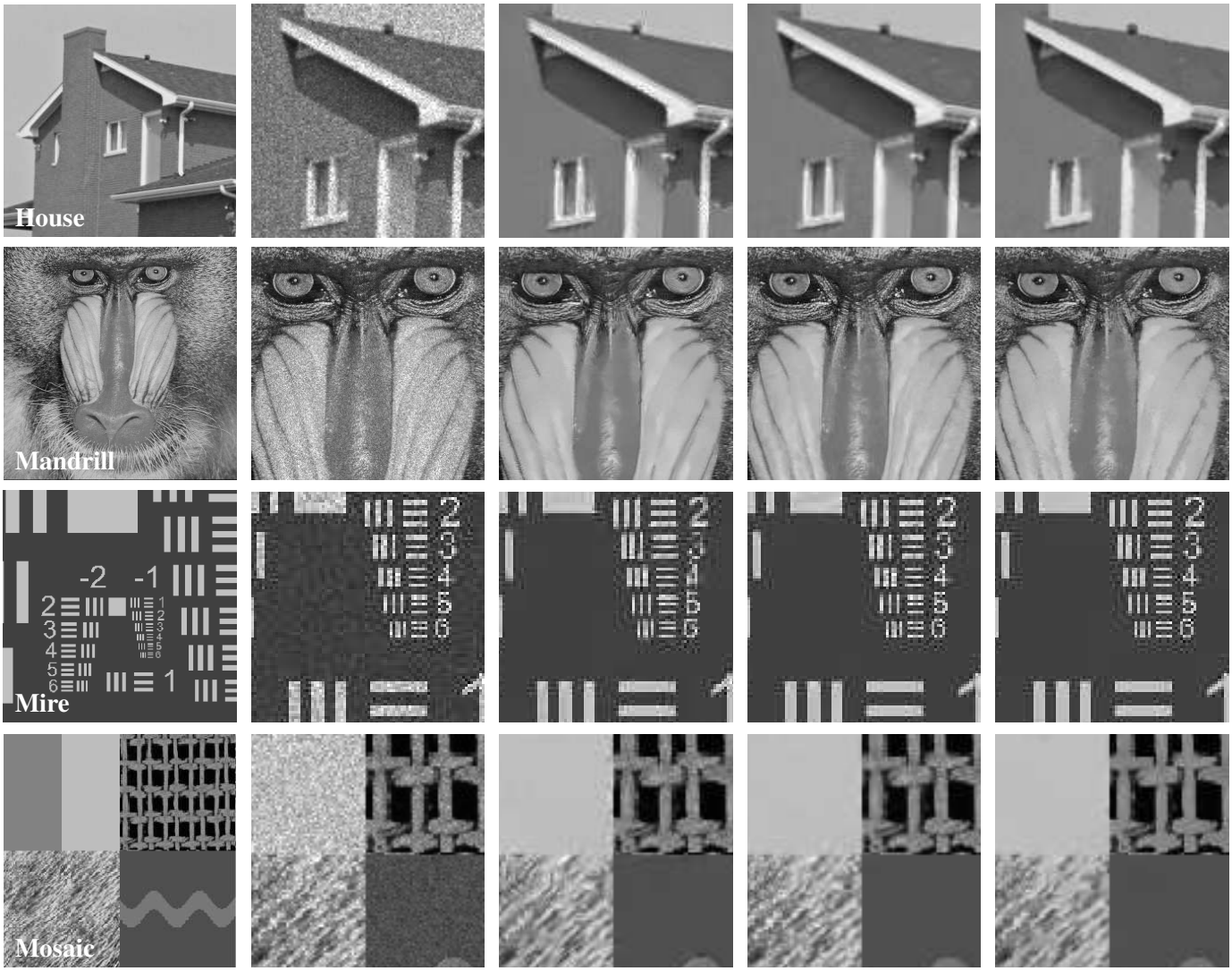

(a) True image (b) Noisy image (c) It. PPB filter (d) SAR-BM3D (e) NL-SAR

Fig. 5. Illustration on denoising scalar (intensity) simulated images. (a) True image. (b) Noisy image (L=16). (c) It. PPB filter. (d) SAR-BM3D. (e) Our result.

2.3. PolSAR images

Figures 14 to 20 compare the performance of NL-SAR with IDAN [Vasile et al., 2006] and refined Lee [Lee et al., 2003] filters on PolSAR data. A wide diversity of images are considered, from high-resolution aerial data (figure 14, 13, 15, 16) to low-resolution aerial data (figure 17), with vegetation areas and urban areas. In order to provide some insight into estimated polarimetric properties, figures 19 and 20 display the H/α polarimetric decompositions.

2.4. PolInSAR images

Figure 21 shows that NL-SAR can also be applied successfully to a polarimetric interferometric SAR image over a scene including volumetric media observed at different incidence angles.

Acknowledgments

The authors would like to thank the Centre National d'Études Spatiales, the Office Nationale d'Études et de Recherches Aérospatiales and the Délégation Générale pour l'Armement for providing the RAMSES data, and the German Aerospace Center (DLR) for providing the TerraSAR-X data (project LAN-1746) and the F-SAR data.

Experiments presented in this paper were carried out using the PlaFRIM experimental testbed, being developed under the INRIA PlaFRIM development action with support from LABRI and IMB and other entities: Conseil Régional d'Aquitaine, FeDER, Université de Bordeaux and CNRS (see https://plafrim.bordeaux.inria.fr/).

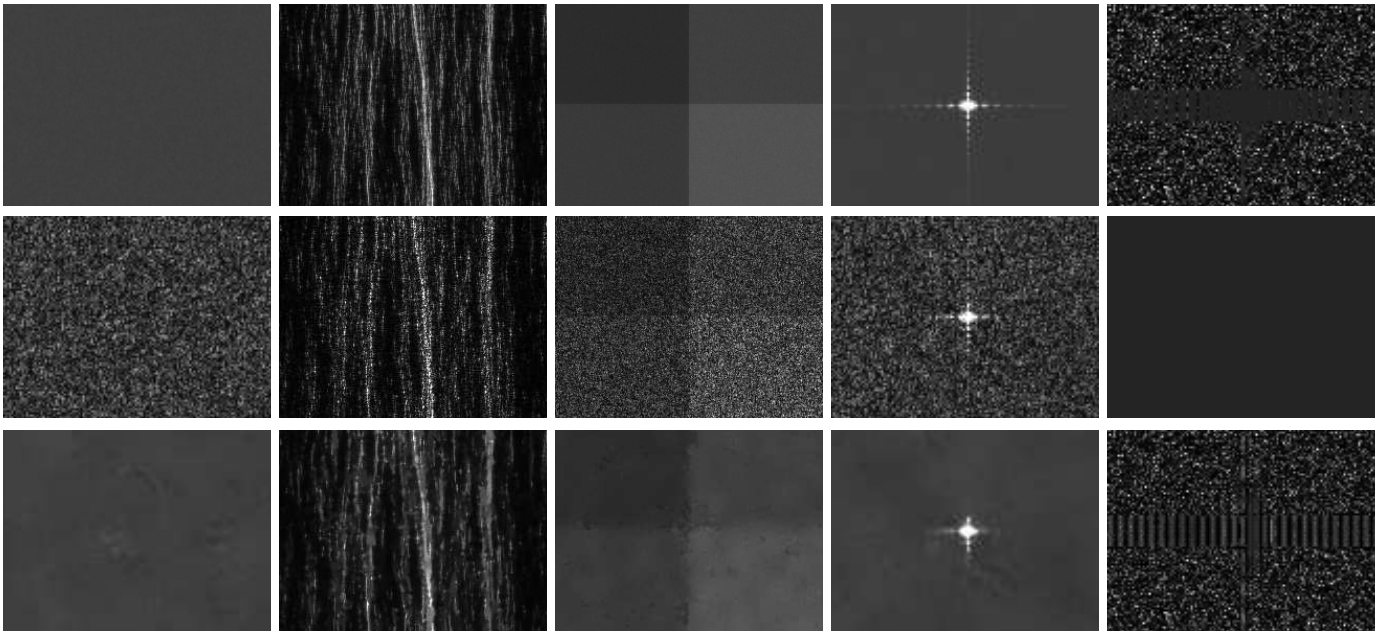

(a) Homogeneous (b) DEM (c) Squares (d) Corner (e) Building

Fig. 6. Restoration of 5 test cases proposed in [Di Martino et al., 2013]: (a) homogeneous region; (b) texture (image of a synthetic fractal DEM); (c) squares image; (d) point target; (e) building (image of residue). From top to bottom: ground truth, version with synthetic speckle and our result.

TABLE II

QUANTITATIVE EVALUATION OF [DI MARTINO ET AL., 2013] WITH COMPARISONS BETWEEN THE PPB FILTER, THE SAR-BM3D FILTER AND OUR APPROACH. FOR EACH CRITERIA, THE TWO BEST APPROACHES ARE HIGHLIGHT IN BOLD.

Measures for Homogeneous

	MoI	MoR	VoR	ENL	ENL*	DG
Clean	1.000	1.003	1.011	445.77	515.57	
Noisy	1.003			0.99	0.99	0
PPB	**1.005**	0.956	**0.824**	**118.81**	**124.46**	**20.12**
SAR-BMD3D	0.985	**0.975**	0.813	90.69	93.65	19.16
NL-SAR	**0.989**	**0.990**	**0.907**	**152.19**	**167.82**	**20.82**

Measures for DEM

	MoI	MoR	VoR	Cx	DG
Clean	1.000	0.984	0.967	2.40	
Noisy	0.987			3.55	0
PPB	**0.984**	**0.911**	**0.558**	2.71	3.63
SAR-BMD3D	**0.953**	0.833	0.418	**2.45**	**5.19**
NL-SAR	0.917	**0.851**	**0.553**	**2.18**	**4.91**

Measures for Squares

	ES (up)	ES (down)	FOM
Clean			0.932
Noisy	0.021	0.105	0.708
PPB	0.080	0.334	**0.800**
SAR-BMD3D	**0.059**	**0.221**	**0.826**
NL-SAR	**0.079**	**0.234**	0.677

Measures for Corner

	CNN	CBG
Clean	7.18	30.54
Noisy	7.19	30.52
PPB	**5.70**	27.29
SAR-BMD3D	**6.83**	**29.55**
NL-SAR	5.57	**33.59**

Measures for Building

	CDR	BS
Clean	59.88	
Noisy	59.87	0.12
PPB	**58.84**	**5.99**
SAR-BMD3D	**59.86**	**1.47**
NL-SAR	63.90	11.74

References

[Deledalle et al., 2009] Deledalle, C., Denis, L., and Tupin, F. (2009). Iterative Weighted Maximum Likelihood Denoising with Probabilistic Patch-Based Weights. *IEEE Trans. on Image Processing*, 18(12):2661–2672.

[Deledalle et al., 2013] Deledalle, C.-A., Denis, L., Tupin, F., Reigber, A., and Jäger, M. (2013). NL-SAR: a unified Non-Local framework for resolution-preserving (Pol)(In)SAR denoising.

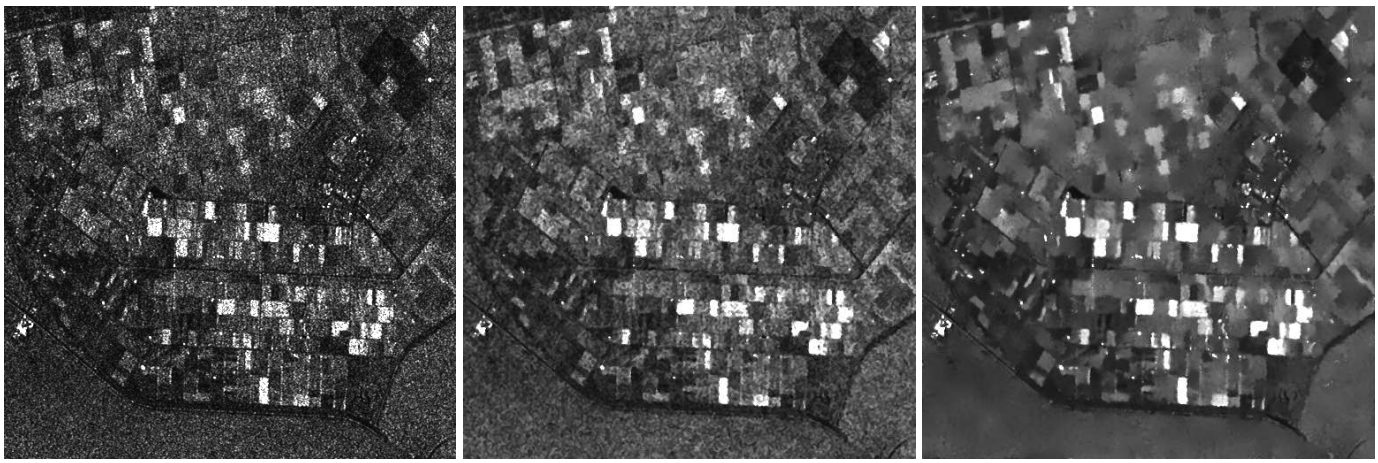

(a) Input image (b) IDAN (c) NL-SAR

Fig. 7. Restoration of an ERS-1 image near Lelystadt (Netherlands) ©ESA: (a) original image; (b) speckle reduction with IDAN; (c) speckle reduction with NL-SAR.

(a) Input image (b) IDAN (c) NL-SAR

Fig. 8. Restoration of a TerraSAR-X image near Toulouse (France) ©DLR: (a) original image; (b) speckle reduction with IDAN; (c) speckle reduction with NL-SAR.

[Di Martino et al., 2013] Di Martino, G., Poderico, M., Poggi, G., Riccio, D., and Verdoliva, L. (2013). Benchmarking framework for SAR despeckling. *to appear in IEEE Trans. on Geoscience and Remote Sensing*.

[Kervrann and Boulanger, 2008] Kervrann, C. and Boulanger, J. (2008). Local Adaptivity to Variable Smoothness for Exemplar-Based Image Regularization and Representation. *International Journal of Computer Vision*, 79(1):45–69.

[Lee, 1983] Lee, J. (1983). Digital image smoothing and the sigma filter. *Computer Vision, Graphics, and Image Processing*, 24:255–269.

[Lee et al., 2003] Lee, J., Cloude, S., Papathanassiou, K., Grunes, M., and Woodhouse, I. (2003). Speckle filtering and coherence estimation of polarimetric SAR interferometry data for forest applications. *IEEE Trans. on Geoscience and Remote Sensing*, 41(10 Part 1):2254–2263.

[Lee et al., 2009] Lee, J.-S., Wen, J.-H., Ainsworth, T. L., Chen, K.-S., and Chen, A. J. (2009). Improved sigma filter for speckle filtering of SAR imagery. *IEEE Trans. on Geoscience and Remote Sensing*, 47(1):202–213.

[Parrilli et al., 2012] Parrilli, S., Poderico, M., Angelino, C. V., and Verdoliva, L. (2012). A nonlocal SAR image denoising algorithm based on llmmse wavelet shrinkage. *IEEE Trans. on Geoscience and Remote Sensing*, 50(2):606–616.

[Vasile et al., 2006] Vasile, G., Trouvé, E., Lee, J., and Buzuloiu, V. (2006). Intensity-driven adaptive-neighborhood

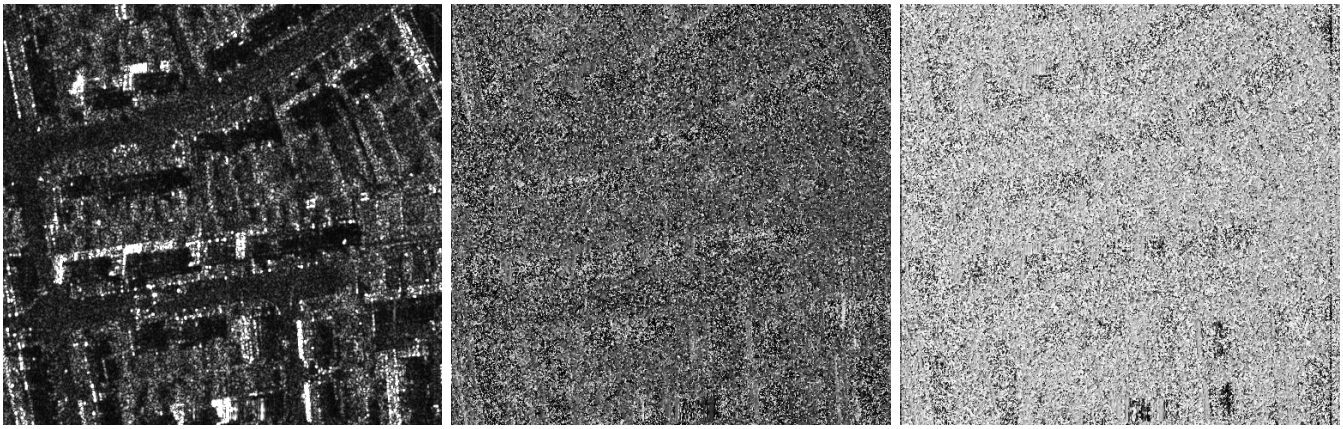

(a) Amplitude (b) Phase (c) Coherence

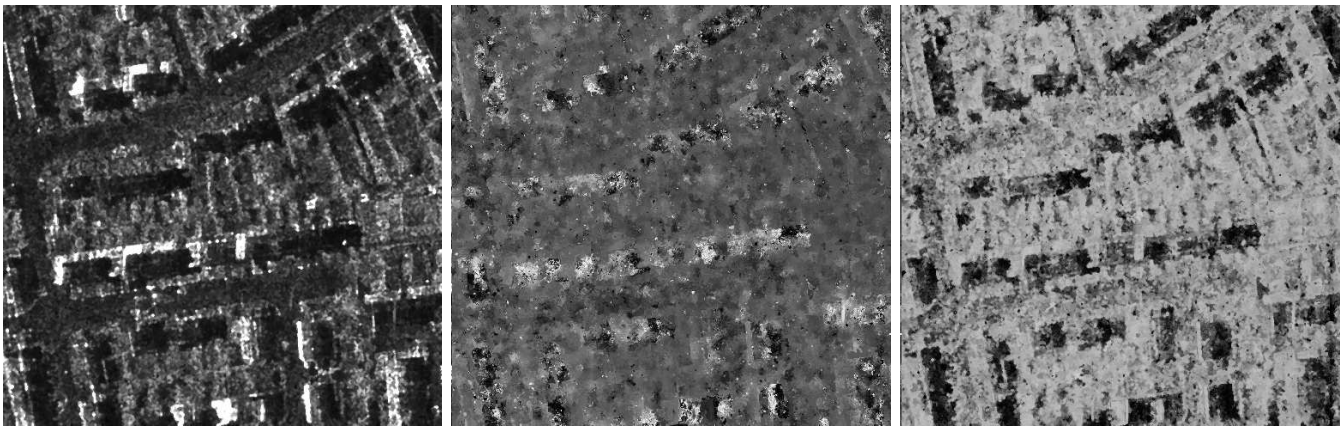

(d) IDAN

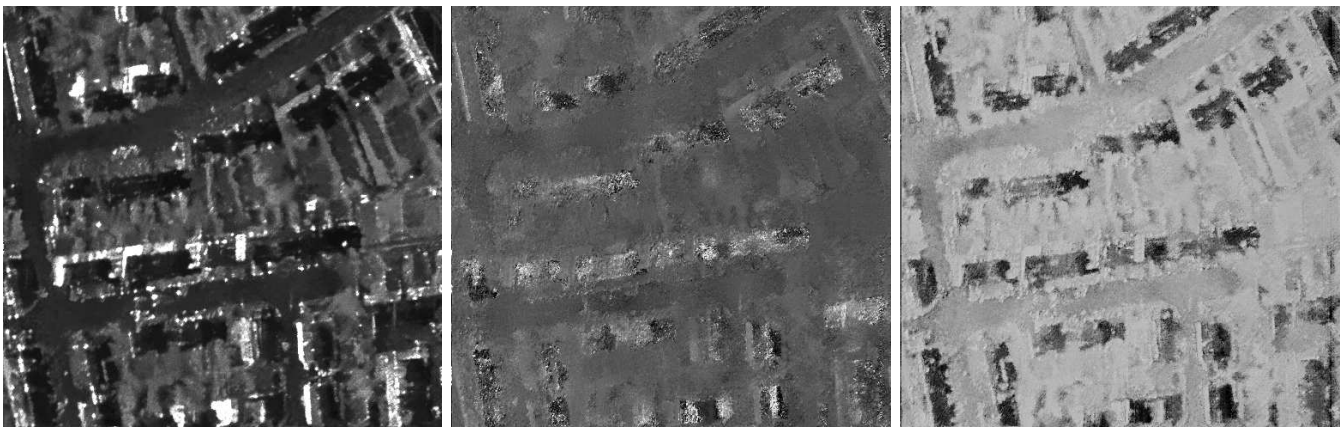

(e) NL-SAR

Fig. 9. Restoration of an interferometric RAMSES image of Cheminot (France) ©ONERA: (a,b,c) original amplitude, phase and coherence images; (d) estimation with IDAN; (e) estimation with NL-SAR.

technique for polarimetric and interferometric SAR parameters estimation. *IEEE Trans. on Geoscience and Remote Sensing*, 44(6):1609–1621.

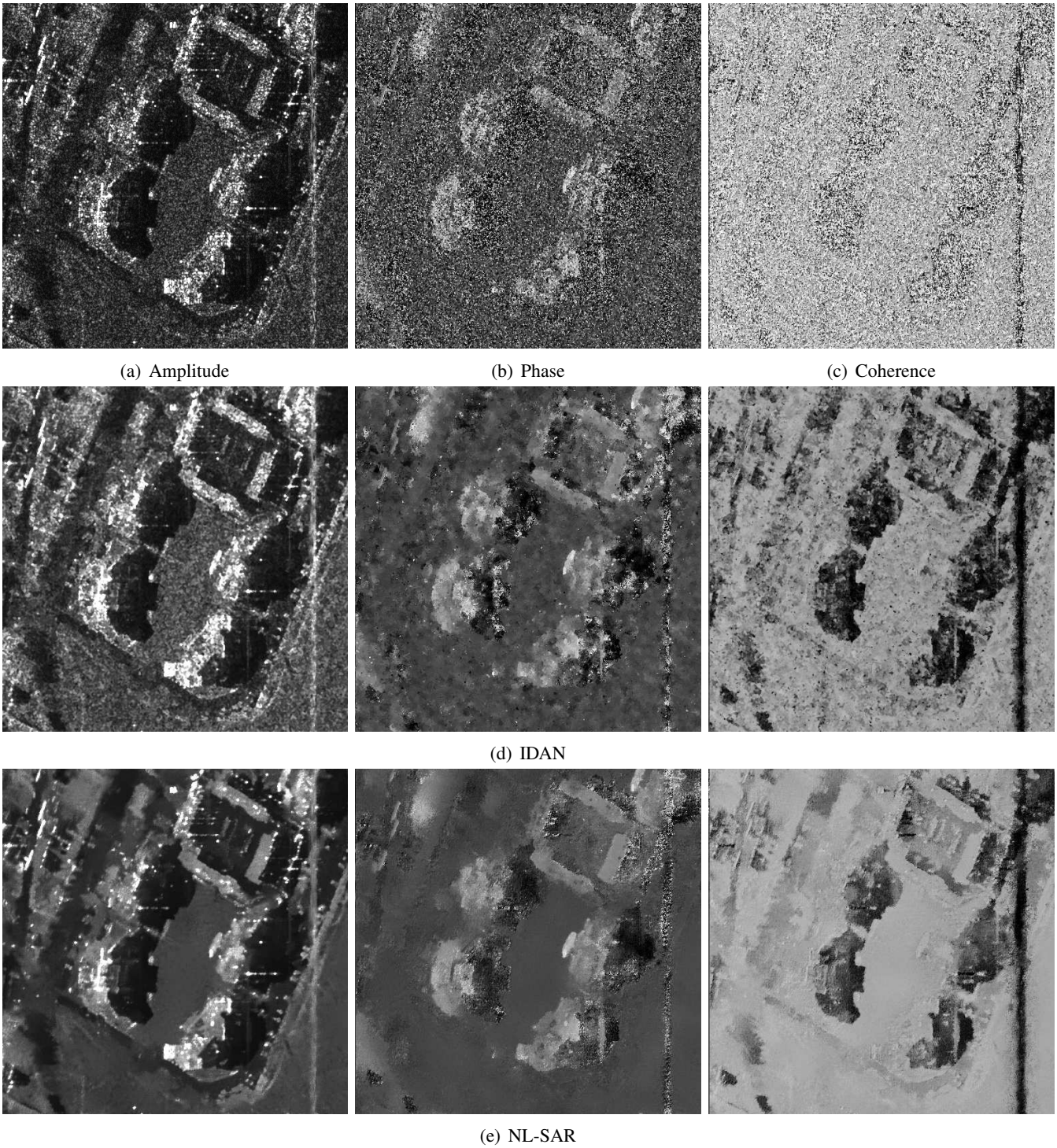

(a) Amplitude (b) Phase (c) Coherence

(d) IDAN

(e) NL-SAR

Fig. 10. Restoration of an interferometric RAMSES image of Bayard (France) ©ONERA: (a,b,c) original amplitude, phase and coherence images; (d) estimation with IDAN; (e) estimation with NL-SAR.

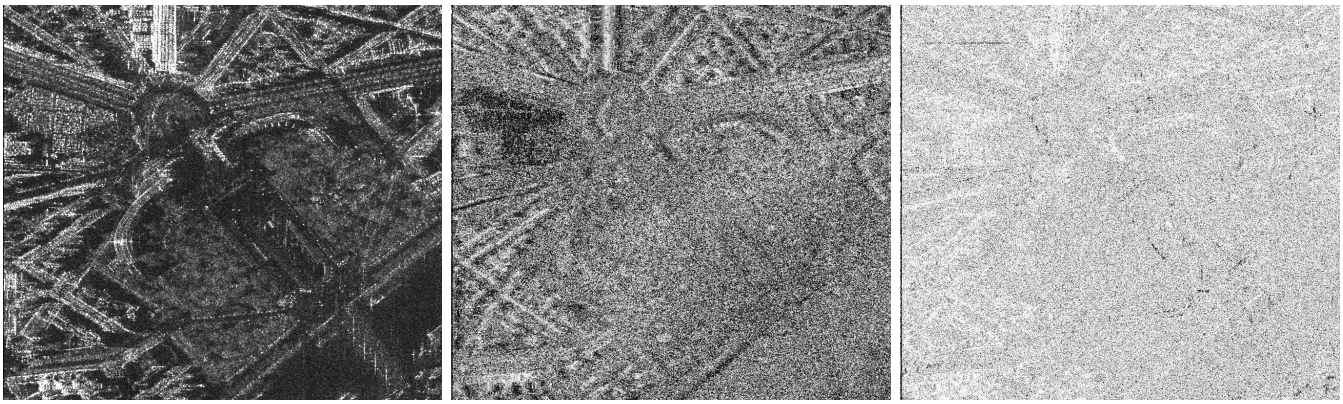

(a) Amplitude (b) Phase (c) Coherence

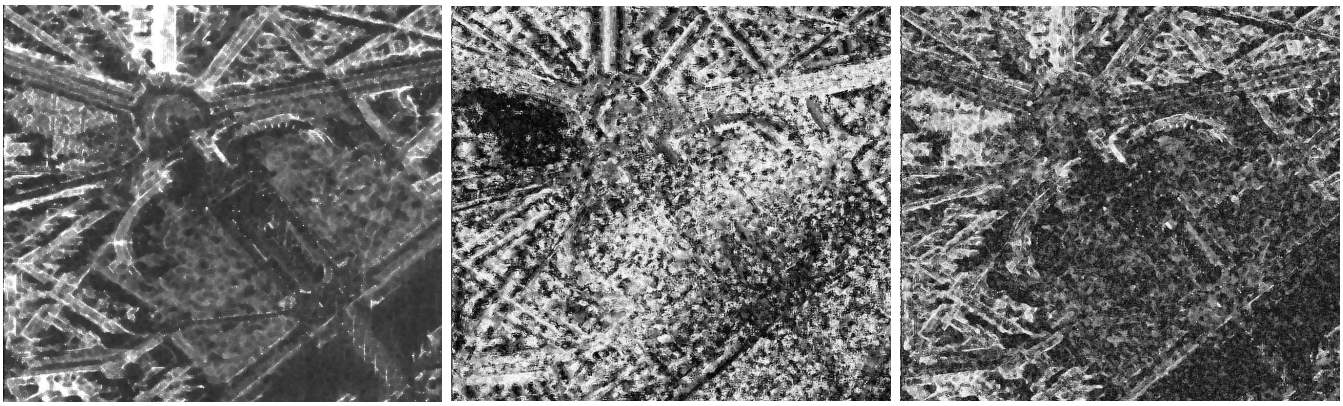

(d) Refined Lee

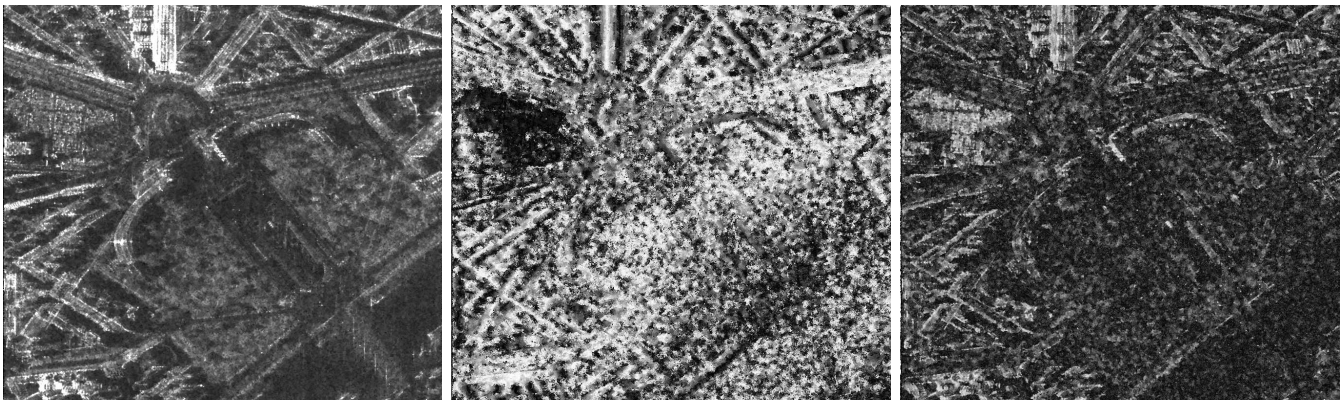

(e) IDAN

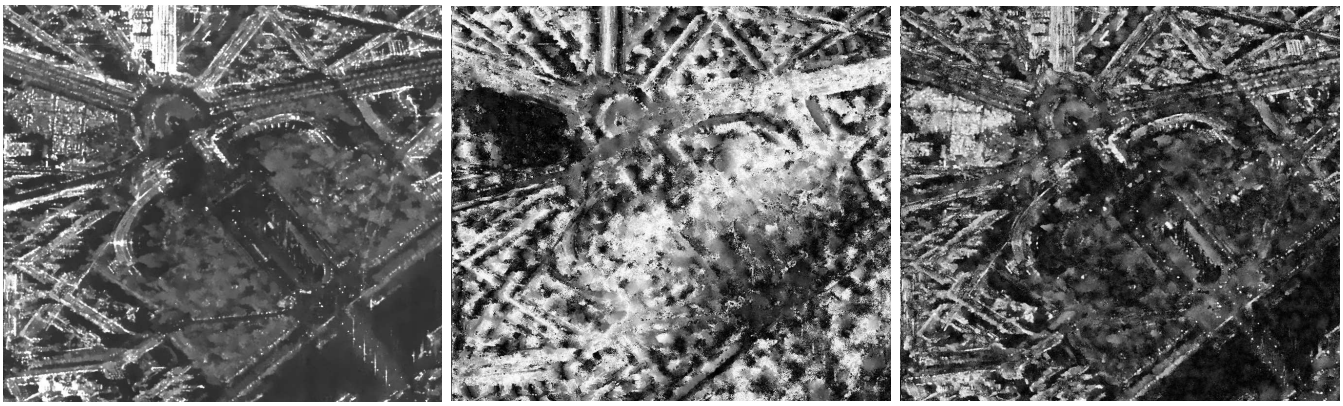

(f) NL-SAR

Fig. 11. Restoration of an interferometric TerraSAR-X image of Paris (France) ©DLR: (a,b,c) original amplitude, phase and coherence images; (d) with the refined Lee filter; (e) estimation with IDAN; (f) with NL-SAR.

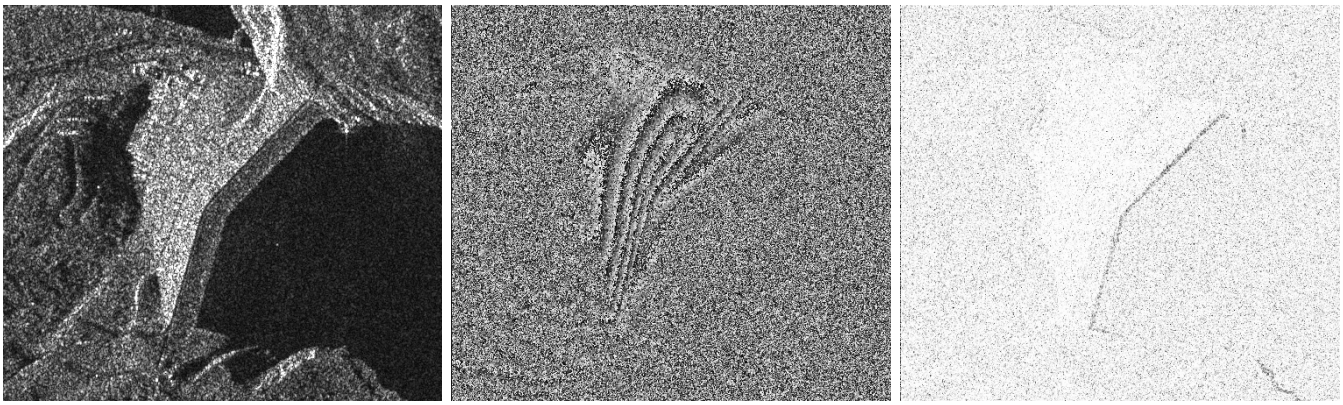

(a) Amplitude (b) Phase (c) Coherence

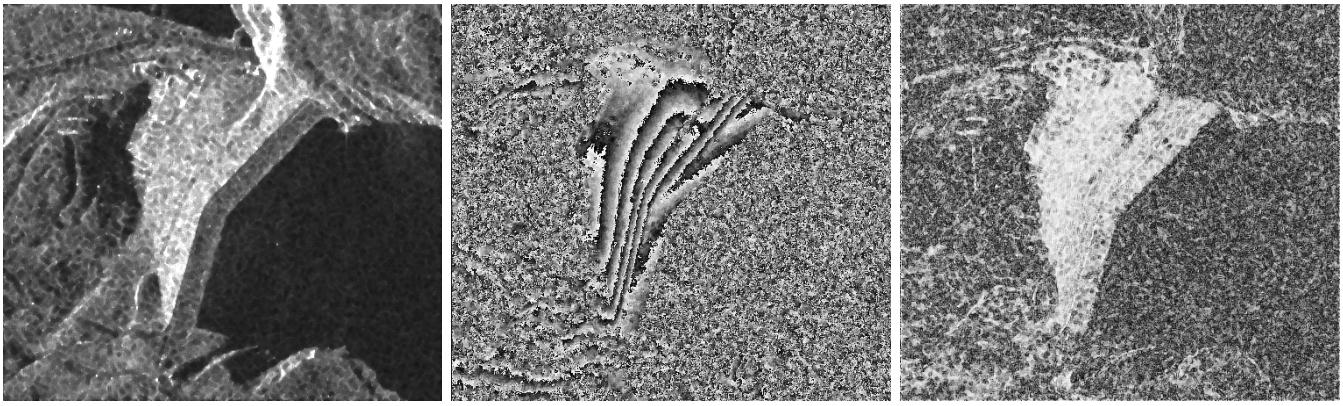

(d) Refined Lee

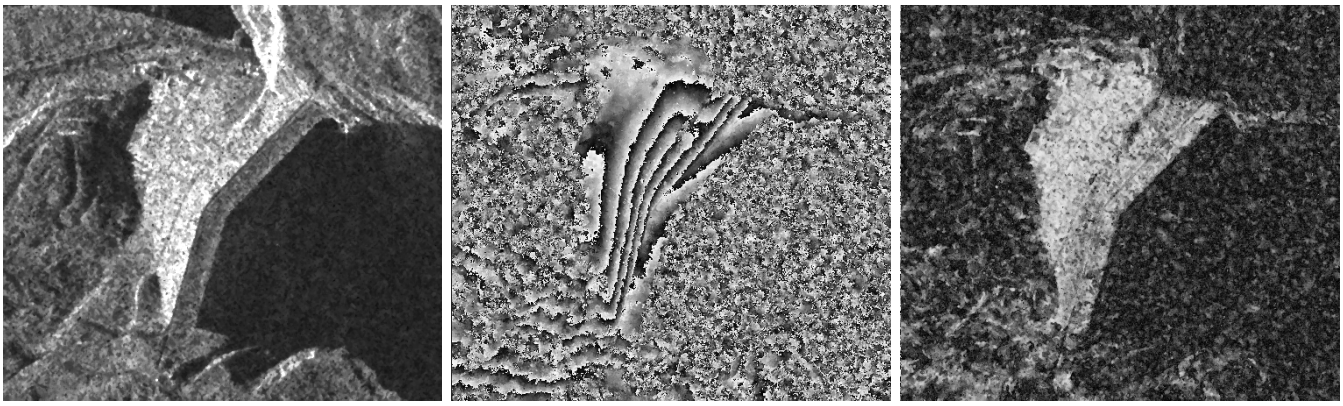

(e) IDAN

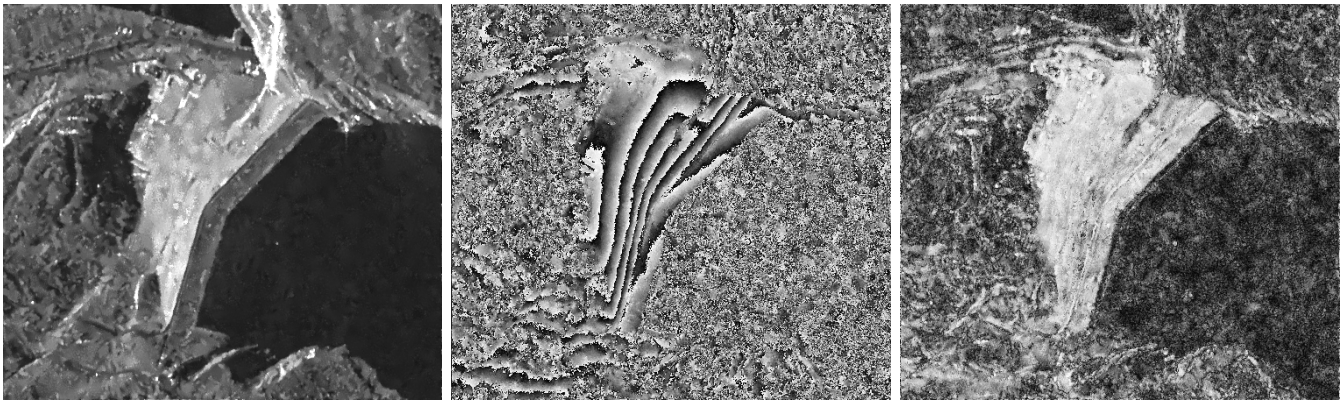

(f) NL-SAR

Fig. 12. Restoration of an interferometric TerraSAR-X image of the Serre-Ponçon dam (France) ©Astrium: (a,b,c) original amplitude, phase and coherence images; (d) with the refined Lee filter; (e) estimation with IDAN; (f) with NL-SAR.

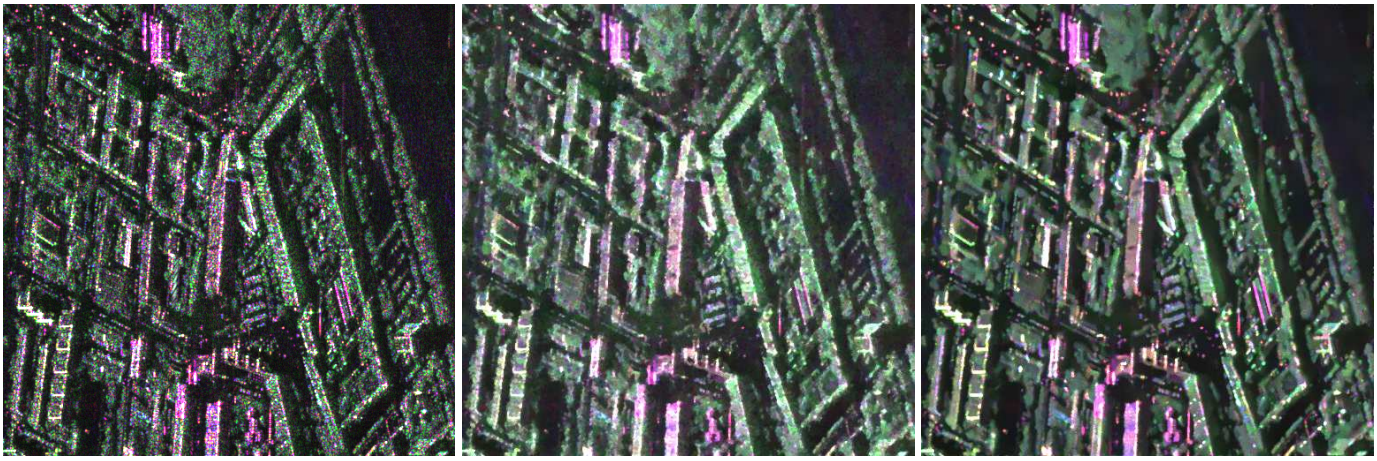

(a) Input image (b) IDAN (c) NL-SAR

Fig. 13. Restoration of a polarimetric E-SAR image of Dresden ©DLR: (a) original image; (b) speckle reduction with IDAN; (c) speckle reduction with NL-SAR.

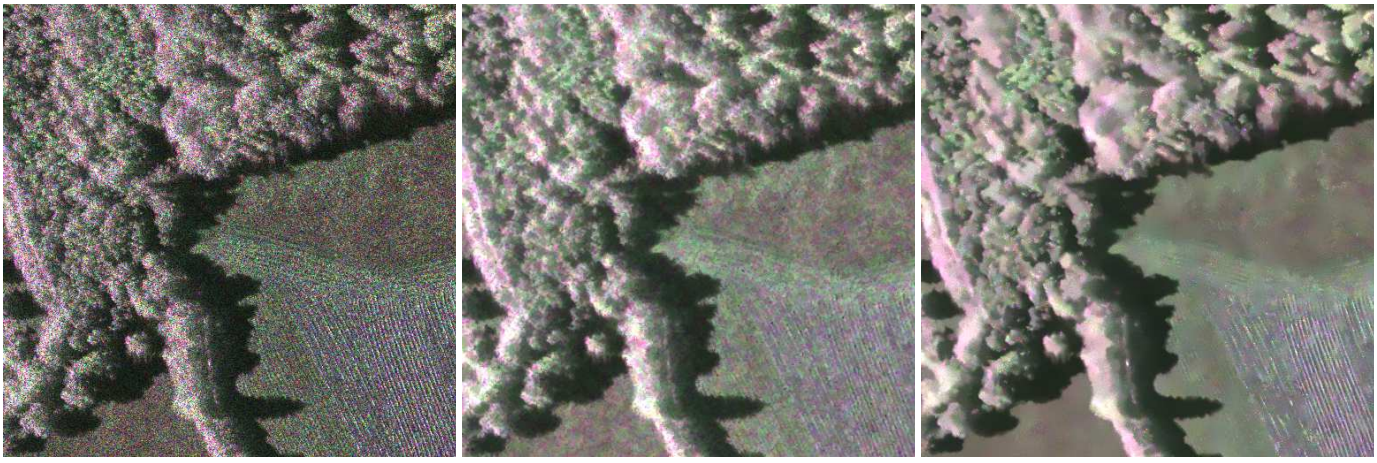

(a) Input image (b) IDAN (c) NL-SAR

Fig. 14. Restoration of a polarimetric F-SAR image near Kaufbeuren (Germany) with complex information (vegetation and fields) ©DLR: (a) original image; (b) speckle reduction with IDAN; (c) speckle reduction with NL-SAR.

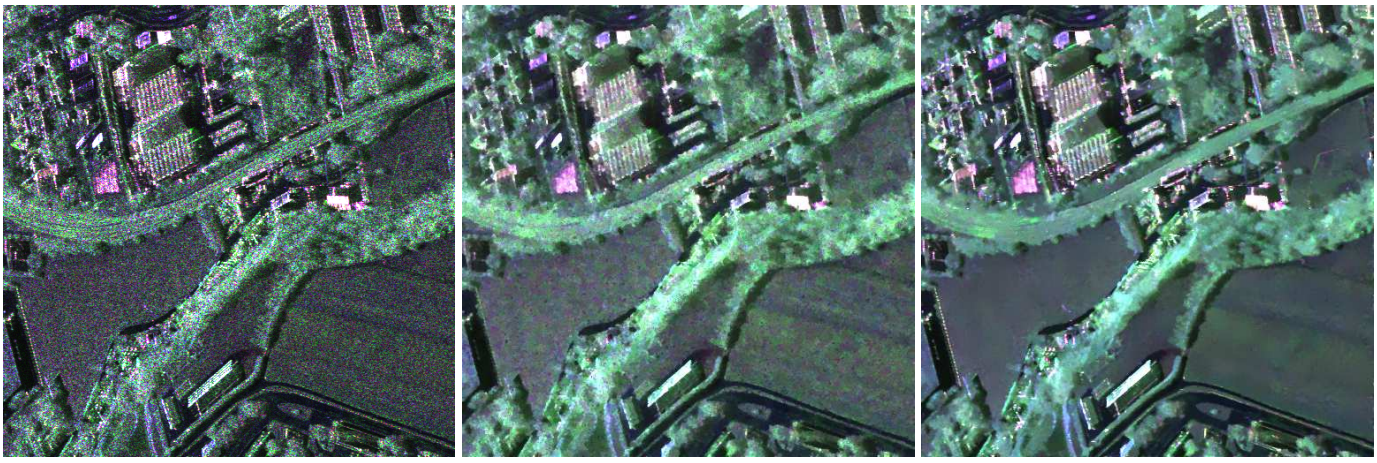

(a) Input image (b) IDAN (c) NL-SAR

Fig. 15. Restoration of a polarimetric F-SAR image near Kaufbeuren (Germany) ©DLR: (a) original image; (b) speckle reduction with IDAN; (c) speckle reduction with NL-SAR.

(a) Input image (b) IDAN (c) NL-SAR

Fig. 16. Restoration of a polarimetric F-SAR image near Kaufbeuren (Germany) ©DLR: (a) original image; b) speckle reduction with IDAN; (c) speckle reduction with NL-SAR.

(a) Input image (b) IDAN (c) NL-SAR

Fig. 17. Restoration of a polarimetric AIRSAR image in L-band of San Francisco (California) ©NASA-JPL-Caltech: (a) original image; (b) speckle reduction with IDAN; (c) speckle reduction with NL-SAR.

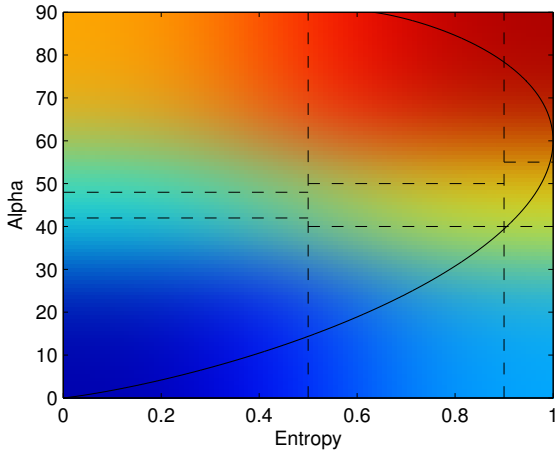

Fig. 18. Colormap used in the H/α based classification

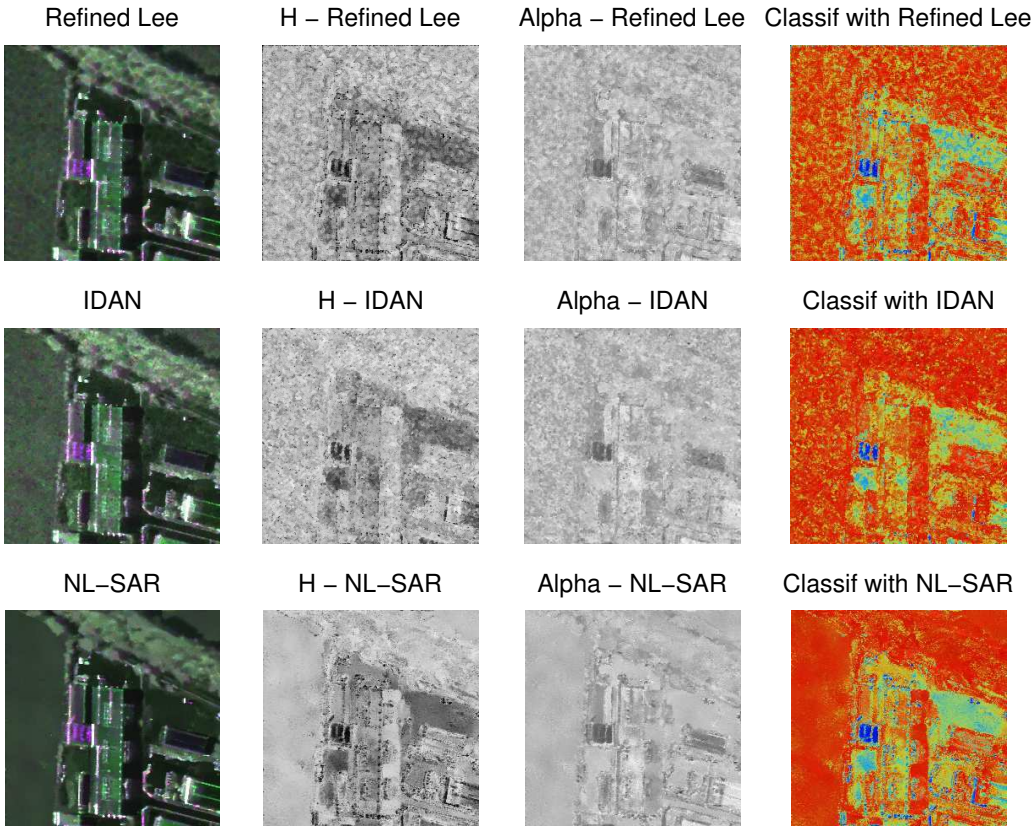

Fig. 19. Classification based on H/α decomposition of an image of Kaufbeuren (Germany) sensed by F-SAR ©DLR. Color labels are given by Fig. 18

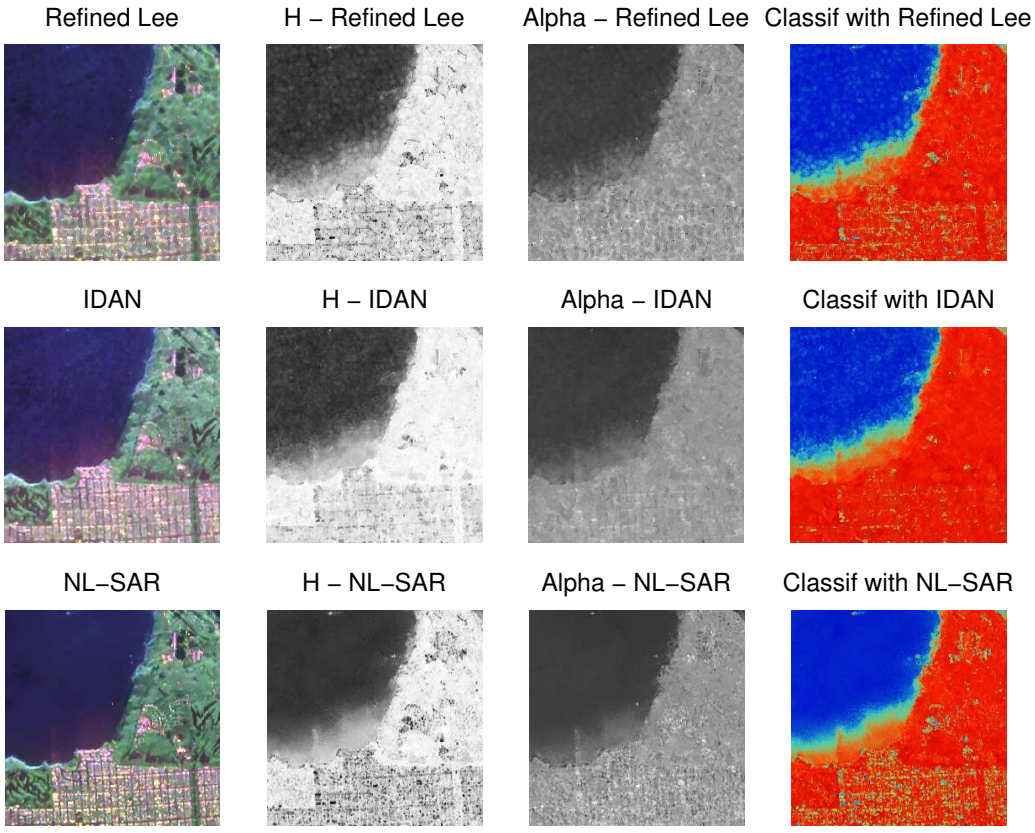

Fig. 20. Classification based on H/α decomposition of an image of San Francisco (USA) sensed by AIRSAR ©NASA-JPL-Caltech. Color labels are given by Fig. 18

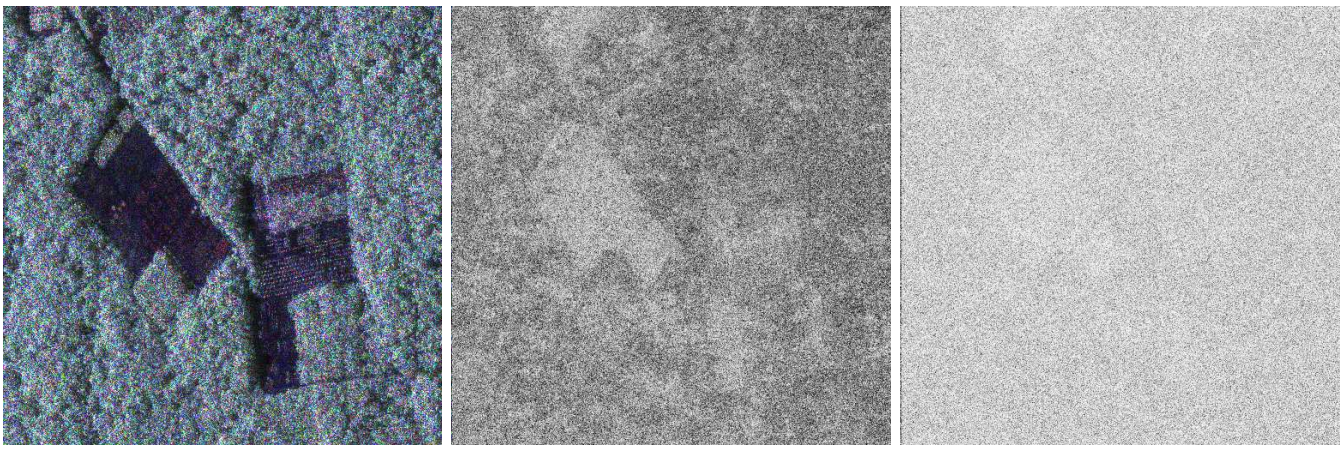

(a) Polarimetry (b) Phase (c) Coherence

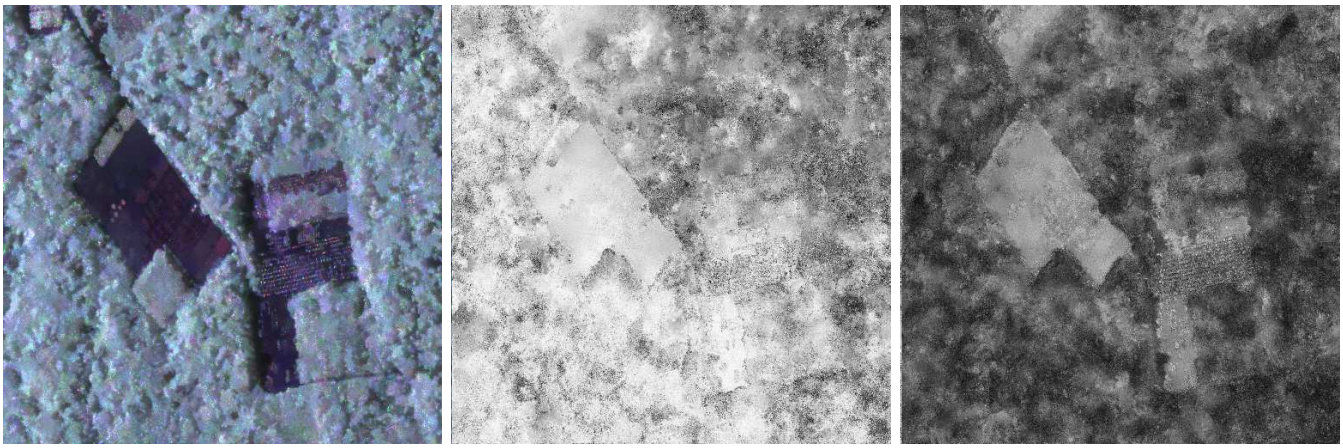

(d) NL-SAR

Fig. 21. Restoration of a polarimetric interferometric L-band TropiSAR image of Paracou (Guyane, France) ©ESA: (a,b,c) original polarimetric, phase and coherence images; (d) estimation with NL-SAR.